AAS 21-707

EARTH-MOON MULTI-BODY ORBITS TO FACILITATE CISLUNAR SURVEILLANCE ACTIVITIES

Maaninee Gupta[*], Kathleen C. Howell[†], and Carolin Frueh[‡]

As human interest expands outward towards the Moon again, there exists a growing focus on Space Domain Awareness to effectively regulate and track objects in the cislunar region. This investigation explores orbits in the Circular Restricted Three-Body Problem that offer behaviors that are favorable to adequately survey cislunar space between the Earth and the Moon. Resonant orbits that provide repeating geometries in an operationally stable environment are introduced. Poincaré maps are employed to leverage invariant manifolds associated with libration point orbits for transfer trajectory design. Access between the lunar vicinity and the geostationary region is facilitated via the proposed orbits.

INTRODUCTION

One of the biggest challenges currently facing the astrodynamics community is the expanse of space debris clouding the vicinity of the Earth. Recognizing the significance of the issue, new techniques and methodologies are being proposed and tested to essentially "clean up" space.[1,2] However, even with the advent of these tools and technologies, another outstanding issue has emerged, that is, the availability of orbits that span and adequately survey broader regions of interest. Recently, general cislunar space has emerged for expanded types of future missions, with efforts driven by both military and commercial space interests.[3] This region, defined as the space between the Earth and just beyond the Moon, is expected to see significantly increased activity – not necessarily with debris from defunct spacecraft as in the lower-Earth realm – but with active missions and satellites in support of both robotic and human spaceflight operations expanding outward to the Moon. Not surprisingly, increased activity mandates increased surveillance capabilities in cislunar space. Future space traffic pathways include libration point orbits in the Earth-Moon system, as well as other orbits that exist within the context of this multi-body regime. Such orbits are becoming increasingly assessed for future hubs, not only in support of lunar missions, but also to maintain constant surveillance and vigilance in circumlunar space.

To address the challenges of increased cislunar activity, it is useful to consider additional types of orbits that may offer surveillance of the entire cislunar space, as well as to highlight some localized options. Moreover, the focus is on orbits with repeating geometries under natural dynamical motion, as this particular characteristic is especially favorable for surveillance activities.[4] Resonant

[*]Ph.D. Student, School of Aeronautics and Astronautics, Purdue University, West Lafayette, IN 47906; gupta208@purdue.edu

[†]Hsu Lo Distinguished Professor of Aeronautics and Astronautics, School of Aeronautics and Astronautics, Purdue University, West Lafayette, IN 47907; howell@purdue.edu

[‡]Associate Professor, School of Aeronautics and Astronautics, Purdue University, West Lafayette, IN 47907; cfrueh@purdue.edu

orbits, i.e., orbits in cislunar space that are in resonance with the orbit of the Moon, are one such example from a number of suitable candidates for the complete observation of cislunar space while guaranteeing operational stability. In addition, such orbits are also part of the network of trajectories that link the lunar vicinity with the near-Earth region. The availability of natural dynamical structures in the vicinity of the proposed libration point orbits broadens the solution space of trajectories and also yields local coverage by single vehicles or multi-spacecraft formations. A sample transfer option also illustrates recurring channels connecting the lunar far side to the near side of the Moon and, thus, to the geostationary region in a multi-body environment.

DYNAMICAL MODEL

This investigation leverages the Circular Restricted Three-Body Problem (CR3BP) in the computation of baseline orbits relevant to this investigation. The CR3BP is an autonomous dynamical model that incorporates the gravitational influences of two planetary bodies that can be a planet-moon or a Sun-planet pair. The Earth and the Moon produce the greatest levels of acceleration on a spacecraft traversing the cislunar region and, thus, these are the two bodies that comprise the model in this analysis.[2] The Earth and the Moon, termed the primaries and denoted as P_1 and P_2, respectively, are assumed to be point masses orbiting their mutual barycenter in circular orbits. The third body represents a smaller body of infinitesimal mass relative to the masses of the primaries and is denoted as P_3. The CR3BP allows the motion of the third body, the spacecraft, to be modeled under the influence of P_1 and P_2. A rotating frame based in the motion of the primaries is adopted to describe the motion of the spacecraft governed by the two bodies. This rotating frame moves at a constant rate, $\dot{\theta}$, relative to an inertial frame, and this rate is equal to the mean motion of the system. Figure 1 represents the orientation of the rotating reference frame, denoted $\hat{x}$-$\hat{y}$-$\hat{z}$, relative to the inertial reference frame, denoted $\hat{X}$-$\hat{Y}$-$\hat{Z}$, with both frames centered on the system barycenter, B.

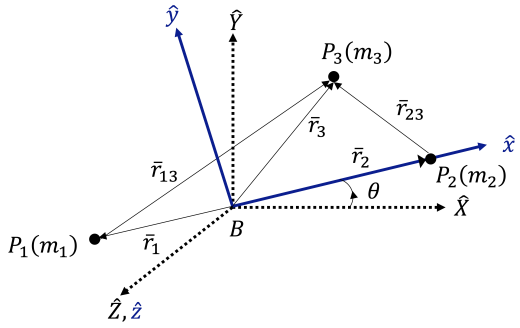

Figure 1. Schematic of the CR3BP inertial and rotating frames.

The equations of motion that represent the motion of P_3 are, by convention, nondimensional. As expressed in the P_1-P_2 rotating frame, the equations of motion are represented as,

$$\ddot{x} - 2\dot{y} = \frac{\partial U^*}{\partial x}, \quad \ddot{y} + 2\dot{x} = \frac{\partial U^*}{\partial y}, \quad \ddot{z} = \frac{\partial U^*}{\partial z} \tag{1}$$

The quantity U^* is the pseudo-potential function, expressed as,

$$U^* = \frac{1-\mu}{r_{13}^3} + \frac{\mu}{r_{23}^3} + \frac{x^2+y^2}{2} \tag{2}$$

where μ is the system mass parameter evaluated as $\mu = \frac{m_2}{m_1+m_2}$, and is roughly equal to 0.01215 for the Earth-Moon system. Additionally, r_{13} and r_{23} denote the nondimensional distances between the Earth and the spacecraft and the Moon and the spacecraft, respectively. The coordinates (x, y, z) correspond to the nondimensional position of the spacecraft relative to the system barycenter in the Earth-Moon rotating frame; similarly, $(\dot{x}, \dot{y}, \dot{z})$ represents the velocity components of the spacecraft as viewed in the rotating frame. Five equilibrium solutions that are termed the libration points or the Lagrange points exist in the CR3BP, denoted as L_i for $i = 1, ..., 5$. Although a closed-form solution does not exist for the equations of motion in the CR3BP, one integral of the motion aids numerical analyses. This quantity is termed the Jacobi constant and is computed as a function of the pseudo-potential and the velocity magnitude for P_3 in the rotating frame, v, as $C = 2U^* - v^2$. Bounds on the allowable motion of P_3 at a given Jacobi constant value are indicated via three-dimensional Zero Velocity Surfaces (ZVSs) and planar Zero Velocity Curves (ZVCs) in configuration space. Regions that are inaccessible at given energies are termed the *forbidden regions*, and a change in velocity (energy) is necessary to enter these regions.

BACKGROUND

Periodic orbits and quasi-periodic trajectories computed in the CR3BP have widely been investigated and applied towards mission design.[5–7] Examples of well-known orbit families include the Lyapunov and halo orbits originating in the vicinity of the collinear libration points, and families of orbits around P_2, such as the distant prograde orbits (DPOs) and distant retrograde orbits (DROs). There also exist families of resonant orbits in mean motion resonance with the lunar orbit. Such orbits are also widely investigated for their naturally repeating geometries and associated dynamical structures.[8] One of the challenges inherent to the CR3BP is the computation of orbits that are periodic and closed as visualized in the rotating frame. Additionally, initial conditions to construct precisely periodic orbits are not usually available. Consequently, differential corrections processes are necessary to construct periodic orbits and trajectories that adhere to the desired itineraries.

Periodic Orbits in the CR3BP

In the Earth-Moon system, the L_1 and L_2 libration points lie approximately $58,000\ km$ and $64,000\ km$ from the center of the Moon, respectively. As such, orbits originating near these points, such as planar Lyapunov and three-dimensional halo orbits, are often leveraged for trajectory design involving lunar proximity operations.[8,9] Additionally, dynamical channels connecting libration point orbits are available, expanding the range of surveillance in the circumlunar region as well. In this investigation, Lyapunov orbits about the L_1 and L_2 libration points are introduced and later employed in the design of transfer trajectories. Portions of the L_1 and L_2 Lyapunov families of planar orbits appear in Figure 2(a) and Figure 2(b), respectively, as visualized in the Earth-Moon rotating frame. Although the L_1 family extends further towards the Earth, only the orbits possessing values of $y-$amplitude that are similar to the L_2 orbits are plotted here.

The P_2-centered Distant Prograde Orbits (DPOs) are of interest as well since, in configuration space, these orbits bridge the gap between the L_1 and L_2 families, thus, offering connections between the interior and exterior regions of the Earth-Moon system. Figure 2(c) illustrates the planar DPOs in the Earth-Moon rotating frame, with the orbits colored consistent with their Jacobi constant values. In the rotating frame, the shape of the orbits changes significantly with the proximity to the Moon: the lower amplitude DPOs are more 'elliptical' around the Moon, while the higher amplitude members possess more complex geometries with longer periods. As viewed in an Earth-centered

inertial frame, the DPOs remain in the vicinity of the lunar orbit.

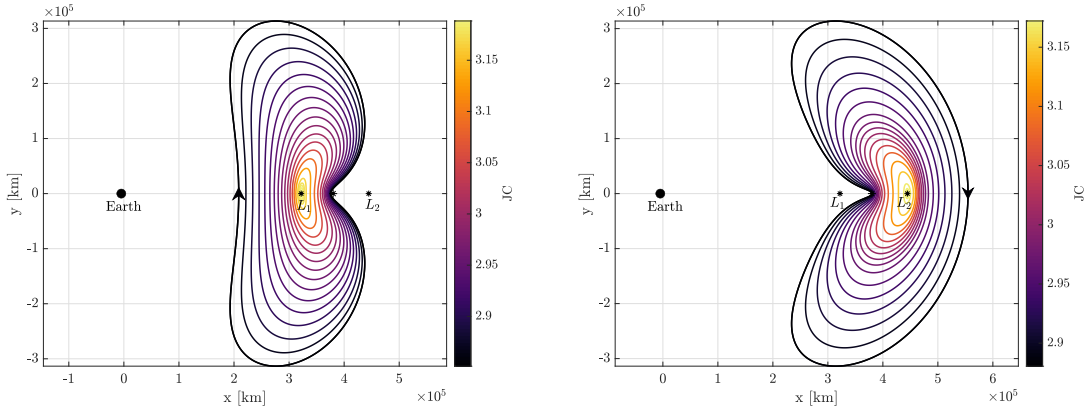

(a) L_1 Lyapunov Orbits

(b) L_2 Lyapunov Orbits

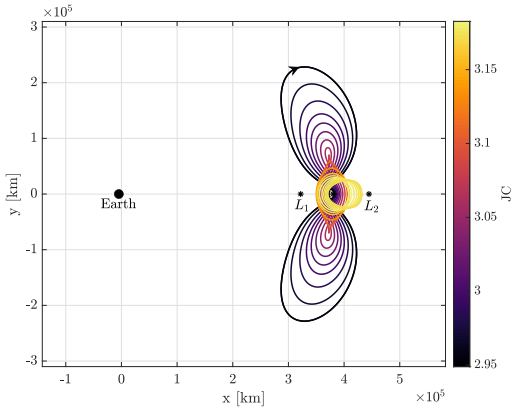

(c) Distant Prograde Orbits

Figure 2. L_1 and L_2 Lyapunov orbits and Distant Prograde Orbits plotted in the Earth-Moon rotating frame.

Evaluating the utility of the orbits supports their application for trajectory design. The eigenvalues of the monodromy matrix, denoted as $(\Phi(t_0 + T, t_0))$, offer insight into the evolution of the flow in the neighborhood of the orbit. Note that, within the CR3BP dynamical model, the six eigenvalues of the monodromy matrix occur in reciprocal pairs. Additionally, one pair of eigenvalues is always equal to unity due to the orbital periodicity. A useful metric to quantify the linear stability of the orbit is the stability index,[10] denoted ν_i and computed as,

$$\nu_i = \frac{1}{2}\left(\lambda_i + \frac{1}{\lambda_i}\right) \tag{3}$$

that results in three unique stability indices for a single periodic orbit. Owing to the unity pair of eigenvalues, at least one stability index for all periodic orbits in the CR3BP equals unity. If any remaining stability indices are greater than unity, the orbit is unstable in a linear sense. Conversely, if the absolute value of the three stability indices is less than or equal to unity, the orbit is linearly stable. Of orbits that are deemed to be linearly unstable, the eigenvalues are also correlated with

time constants for departure from the orbit. Thus, larger magnitudes of the stability index indicate faster departure from the vicinity of the baseline orbit.

For the subsets of the L_1, L_2, and DPO families represented in Figure 2, the evolution of the stability index as a function of the Jacobi constant along the orbit family is plotted in Figure 3(a). Clearly, orbits that are linearly unstable are found in all three families, implying the existence of invariant manifolds that can be employed for rapid departure and arrival from their underlying orbits. Additionally, there is an overlap in the values of Jacobi constant for which orbits from all three families are unstable. This fact enables the construction of cost-free transfers that link the orbits.[11] Also appearing in Figure 3(b) are curves highlighting the evolution of the orbital periods along the L_1 and L_2 Lyapunov families and the DPOs. The shorter period DPOs possessing higher values of Jacobi constant tend to be linearly stable, which limits the availability of natural transfers between the orbits.

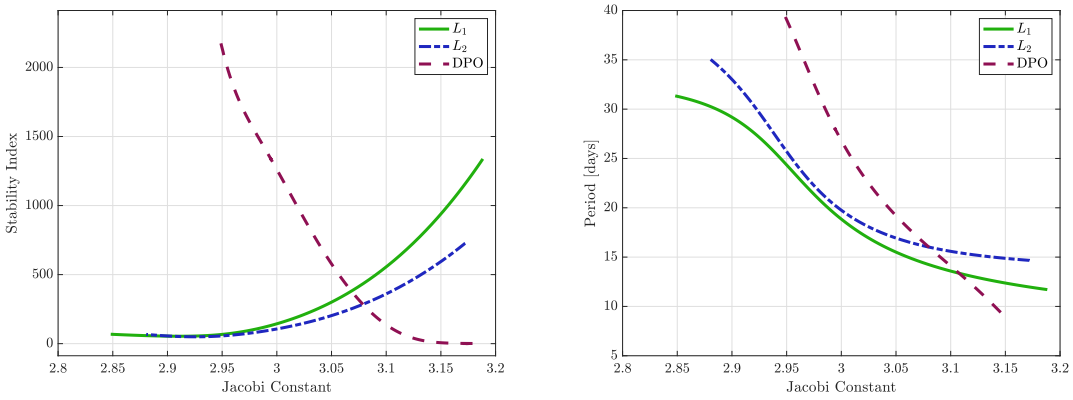

(a) Stability Indices (b) Orbital Period

Figure 3. Stability indices and orbital periods along the families of L_1 and L_2 Lyapunov orbits and DPOs.

Resonant Orbits

Resonant orbits are periodic and are favored because they provide naturally repeating geometries for space-based observations.[12] Historically, resonant orbits have frequently been employed for long-term mission design. In 2008, the Interstellar Boundary Explorer (IBEX) was launched into a highly elliptical Earth orbit with a radius of periapsis approximately equal to $1.5R_E$, where R_E denotes the equatorial radius of the Earth.[13] This low perigee exposed the spacecraft to undesirable amounts of radiation. Additionally, the apogee of the orbit extended nearly to the radius of the lunar orbit, and as a result, repeated corrections were necessary to retain the spacecraft in that orbit. Thus, in 2011, the orbit of IBEX was adjusted and shifted into a 3:1 resonant orbit that would guarantee operational stability for decades, while also raising the perigee to a more suitable radius for avoiding radiation exposure.

Resonant orbits are characterized by their resonance ratio, denoted p:q, which is a simple integer ratio of the orbital periods of the bodies in resonance. A spacecraft orbiting the Earth and in a p:q resonance with the Moon encircles the Earth p times in the interval required for the Moon to complete q revolutions of the Earth. For resonant orbits computed in the Earth-Moon CR3BP,

the ratio of the orbital periods is not a perfect integer, i.e., the spacecraft completes p orbits in approximately the time that the Moon completes q revolutions of the Earth. Resonance ratios with $p > q$ are indicative of *interior* resonances, while ratios with $p < q$ describe *exterior* resonances. Additionally, since periodic orbits in the CR3BP exist as families of solutions that share similar characteristics, so do these resonant orbits. Valuable insight is gained by computing and analyzing families of interior resonant orbits, an inherent advantage of employing the CR3BP as the primary dynamical model in this investigation.

One methodology for the computation of a resonant orbit in the CR3BP relies on first computing its two-body model counterpart.[14] Since the CR3BP incorporates the gravitational influence of the Moon on the spacecraft (P_3), simply propagating the two-body orbit using the CR3BP equations of motion is not sufficient, and the initial conditions for the orbit require adjustment via differential corrections to produce a closed periodic resonant orbit. In addition, employing natural parameter continuation, numerous additional orbits that share similar characteristics and geometries are computed in the CR3BP as well. Orbit families associated with various resonance ratios, such as those illustrated in Figure 4, are computed in the Earth-Moon system. Members in these resonant orbit families are colored according to their value of Jacobi constant. As depicted here, the Jacobi constant scale varies with each family. In general, the availability of orbits possessing different resonance ratios is dependent on the Jacobi constant value. Interior resonant orbits, such as the 3:2 resonant orbits represented in Figure 4(f), can be leveraged to offer complete surveillance of the cislunar region, potentially useful for multiple spacecraft deployed simultaneously or in series.

HIGH ENERGY 2:1 RETROGRADE RESONANT ORBITS

Observations as well as pathways throughout cislunar space are challenging, as this region is large.[15] For observations, there are potential ground-based sensors on both Earth and the Moon, each with advantages and disadvantages. Space-based sensors that might be in Earth orbits or Moon orbits are also likely to be employed. However, to expand the range of options, sensors in cislunar orbits, especially those offering repeating geometries, offer particular advantages. The interior 2:1 retrograde resonance is one example of a resonant orbit family that offers cislunar surveillance opportunities. The orbits in this family possess a characteristic geometry and resonant behavior that results in naturally repeating pathways that link the Earth and the Moon. A subset from this family of orbits is illustrated in Figure 5(a), with each orbit colored by its Jacobi constant value. A spacecraft placed in an orbit from this family completes two revolutions about the Earth in approximately the time that the Moon requires to complete one Earth revolution, evident by visualizing the motion in an Earth-centered inertial frame, as demonstrated in Figure 5(b). The direction of motion indicated by the arrows on a sample orbit in Figure 5(b) illustrates the retrograde nature of these orbits. The dashed curve represents the lunar orbit – the higher the Jacobi constant value, the further the orbit extends towards the orbit of the Moon with an increasing value of its maximum radius relative to the Earth.

Barring the unity stability index for each orbit, ν_3, the evolution of the remaining two stability indices along the 2:1 retrograde resonant orbits is reflected in Figure 6(a) for the same range of Jacobi constants as Figure 5. Given the criteria for linear stability, each orbit in this subset of the family is linearly unstable. Additionally, the variation in the orbital period along the family is not monotonic, as highlighted in Figure 6(b). Orbits with lower Jacobi constant values and, thus, higher energies, correspond to the longest periods and are closer to the linear stability threshold. Overall, the periods remain close to the lunar sidereal period of approximately $27.32\ days$, consistent with

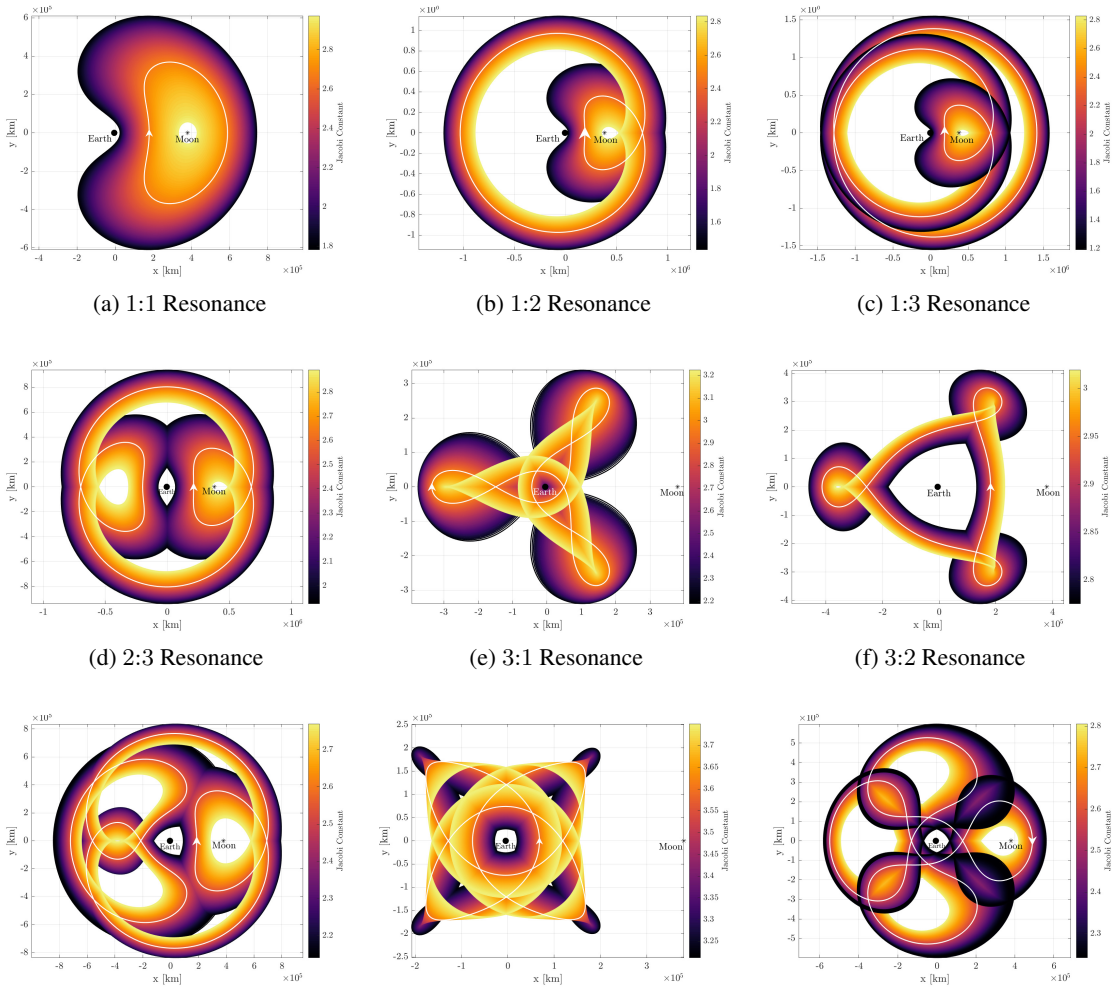

(a) 1:1 Resonance (b) 1:2 Resonance (c) 1:3 Resonance

(d) 2:3 Resonance (e) 3:1 Resonance (f) 3:2 Resonance

(g) 3:4 Resonance (h) 4:1 Resonance (i) 4:3 Resonance

Figure 4. Planar resonant orbit families in the Earth-Moon system. In each family, the orbit in white highlights the direct of motion.

their resonance ratio.

With their unique geometries, several orbits from this family present convenient opportunities for cislunar observation. However, of particular interest are orbits that guarantee natural ballistic access between the Earth and the Moon. A sample orbit from the family, the 2:1 retrograde resonant orbit illustrated in Figure 7 is selected. After departing the lunar vicinity, the orbit approaches the radius of a geosynchronous orbit in the retrograde direction. As a result, access between the vicinity of the Moon and the near-Earth region is offered with every revolution of the orbit. Figure 7(a) illustrates a view of the orbit in the Earth-Moon rotating frame, while the orbit appears in Figure 7(b) as visualized in an Earth-centered inertial frame. The points along the orbit are colored consistently between the two frames in an isochronous fashion, aiding the understanding of the complex geometry that arises in the rotating frame. The period of the orbit is approximately 26 $days$ and, thus, each elliptical lobe that appears in the inertial frame spans about 13 $days$. The orbit possesses a relatively low nondimensional Jacobi constant value of 0.8964. This Jacobi constant corresponds to

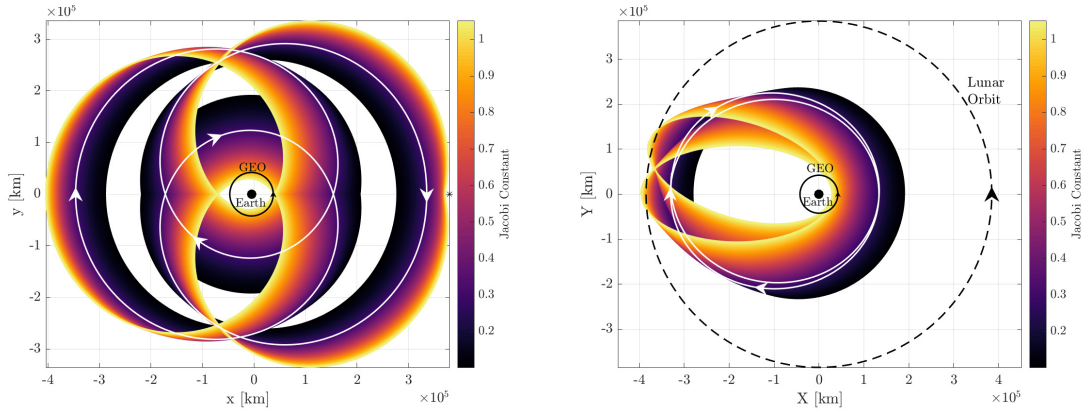

(a) Earth-Moon Rotating Frame (b) Earth-Moon Inertial Frame

Figure 5. Family of 2:1 retrograde resonant orbits in the Earth-Moon system.

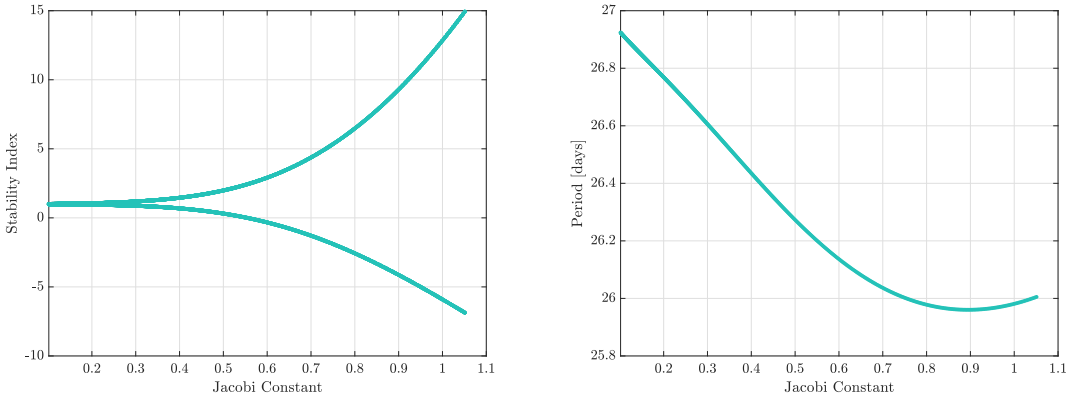

(a) Stability Indices (b) Orbital Period

Figure 6. Stability indices and orbital periods along the family of 2:1 retrograde resonant orbits.

a relatively high orbital energy, not surprising given its size. Additionally, although the resonance ratio is not a perfect integer, the orbit is closed and periodic as observed in the rotating frame.

A distinct feature of the orbit in Figure 7 is the point of closest lunar approach that occurs at the half-period mark on the orbit. Due to the lunar proximity at this location, and since the CR3BP incorporates the gravitational effects of the Moon, the orbit naturally and predictably precesses in the inertial view, and the 'line of apsides' continue to advance in the inertial frame. Notably, this behavior varies in other members of the orbit family represented in Figure 5(b): the orbits with lower values of Jacobi constant possess less eccentric lobes and as a result, those orbits undergo insignificant amounts of precession in their lines of apsides. Furthermore, the 2:1 retrograde resonant orbit highlighted in Figure 7 is defined by a periapse distance exactly equal to the geosynchronous orbit (GEO). To examine the mapping of cislunar space exhibited by this resonance, the initial state associated with the orbit is propagated for approximately 20 revolutions in the rotating frame, corresponding to about $507\ days$. Figure 8(a) demonstrates the evolution of the resulting ballis-

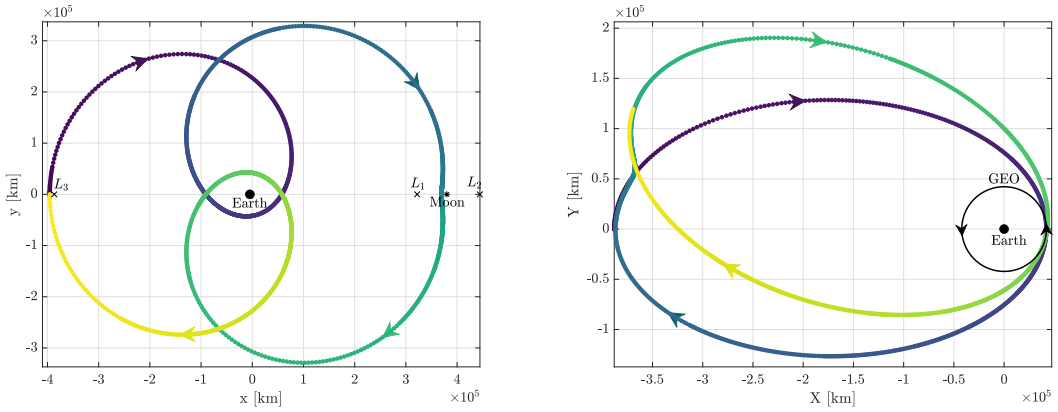

(a) Earth-Moon Rotating Frame (b) Earth-Moon Inertial Frame

Figure 7. A 2:1 planar retrograde resonant orbit computed in the Earth-Moon CR3BP. Typical of resonant orbits, one full revolution of this orbit in the rotating frame yields two revolutions in the inertial frame.

tic trajectory in the rotating frame that clearly resembles the original orbit. In the inertial view in Figure 8(b), it is apparent that propagating for multiple revolutions, this orbit provides a complete surveillance of the cislunar region, supplying recurring prospects for access between the near-Earth region and the lunar vicinity.

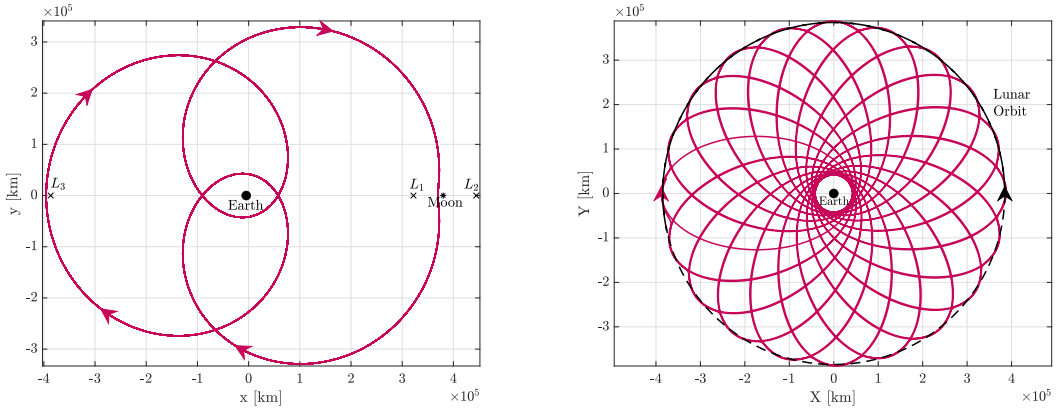

(a) Earth-Moon Rotating Frame (b) Earth-Moon Inertial Frame

Figure 8. A 2:1 retrograde resonant orbit mapping out the cislunar region.

TRANSFER TRAJECTORIES

Spacecraft placed in L_2 Lyapunov or halo orbits enable observations of the far side of the Moon. It is also notable that three-dimensional L_2 halo trajectories offer lines-of-sight to both the Earth and the back side of the Moon simultaneously over the entire orbit.[16] For preliminary examination, consider the planar Lyapunov family. In a planar L_2 orbit, no direct Earth link exists from the lunar back side. By connecting orbits on the L_2 side with their L_1 counterparts, however, continuous observation of both the near and far sides of the Moon is attainable as well. Additionally, such chains

of trajectories suggest one option to compensate for the lack of direct communication channels between the Earth and the lunar far side. Thus, the availability of transfers connecting L_1 and L_2 Lyapunov orbits and the DPOs is investigated. Additionally, the applicability of the 2:1 retrograde resonant orbits for surveillance missions in cislunar space is assessed via the availability of transfers into these orbits. Large cislunar orbits and local libration point orbits possess very different energy levels. The low range of Jacobi constant values for the resonant orbits presents challenges since the existence of natural dynamical structures and periodic orbits at that energy level is limited. Nevertheless, flow from nearby orbits is leveraged and some resulting transfer solutions are introduced to illustrate the links between various types of cislunar orbits.

Natural Transfers between Lyapunov Orbits and Distant Prograde Orbits

Recall from Figure 3(a) that, over a range of Jacobi constant values, the L_1 and L_2 Lyapunov families and the DPOs all possess unstable members. As a result, cost-free transfer solutions linking the orbits are available within that range.[8,11] Such cost-free transfers, termed heteroclinic connections, are natural ballistic trajectories that connect two unstable periodic orbits at the same energy levels. The unstable and stable manifolds associated with the departure and the arrival orbits, respectively, are employed in the computation of heteroclinic connections.[17] Additionally, it is also possible to link two separate heteroclinic connections (L_1-DPO and DPO-L_2, e.g.) to produce *heteroclinic chains* that exhibit the geometries incorporating all of the underlying orbits.

Consider the L_1 and L_2 Lyapunov orbits and the DPO represented in Figure 9(a), all at the same Jacobi constant value of 2.97895. The periods of the three orbits are listed in Table 1, along with the stability index associated with each orbit. It is evident that all the orbits are unstable in a linear sense and, thus, trajectories that naturally depart from and arrive into the orbits are accessible. An additional parameter, termed the cone angle and denoted β, is introduced such that,

$$\beta = tan^{-1}\left(\frac{A_y}{d}\right)$$

where A_y is the orbit amplitude in the y-direction. The value of d varies by orbit type: for L_1 (L_2) Lyapunov orbits, d is evaluated as the distance between the Earth and L_1 (L_2). For the DPOs, the distance is instead measured from the Earth to the Moon. Table 1 also lists the cone angles associated with each orbit. The cone angle, β, aids in assessing the size of these libration point orbits within the context of a cone with the vertex at the Earth. Within cislunar space, an approximately 30° cone of observation from the Earth to the Moon is of particular interest for surveillance activities, as noted in recent announcements of the 'Cislunar Highway Patrol System' proposed by AFRL.[18]

Table 1. Characteristics of the selected orbits at $C = 2.97895$.

Orbit	Period (days)	Stability Index	Cone Angle (°)
L_1 Lyapunov	20.93	102.237	22.13
L_2 Lyapunov	21.79	79.811	16.57
DPO	31.57	1550.860	24.66

To produce arcs that depart from the L_1 Lyapunov orbit, trajectories along its unstable manifold are numerically produced. Similarly, for arrival into the L_2 Lyapunov orbit, trajectories that are asymptotic to its stable manifold are computed. Additionally, to demonstrate the existence of heteroclinic chains that leverage flow associated with the DPO, trajectories along its stable and unstable

manifold are determined as well. Although these trajectories are significantly tangled in configuration space, insight into the behavior of the flow near the three orbits is apparent from Poincaré maps. A surface of section is defined with the hyperplane $\Sigma : x = 1 - \mu$, corresponding to the location of the Moon along the $\hat{x}$-axis. The intersections of the trajectories with the hyperplane are recorded and appear in Figure 9(b) as projected along the $y - \dot{y}$ axes. Returns of trajectories along the unstable manifold of the L_1 Lyapunov orbit are plotted in magenta; returns of trajectories on the stable manifold of the L_2 Lyapunov orbit appear in blue. For the DPO, the stable manifold crossings are plotted in teal, and finally, the unstable manifold crossings are plotted in yellow. Note that, since the trajectories are all planar and the Jacobi constant value is fixed across the map, the full 4-dimensional state corresponding to each return is known.

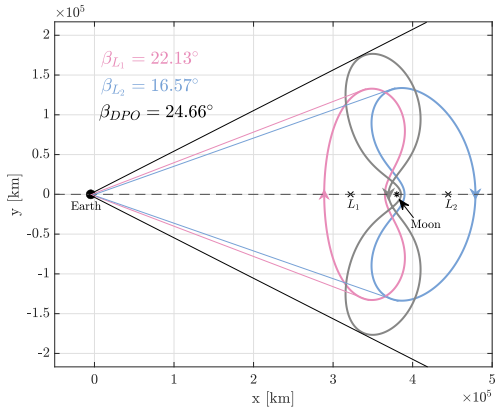

(a) Selected Orbits and Cone Angles

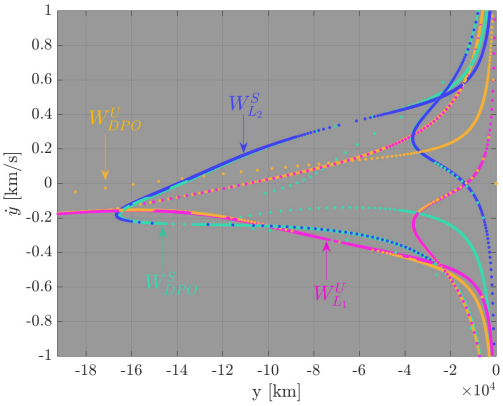

(b) Poincaré Section

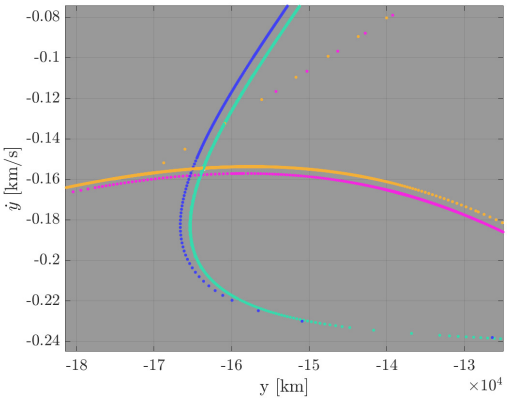

(c) Zoomed-in View

Figure 9. Selected orbits and Poincaré section with returns of trajectories on invariant manifolds of the orbits.

Intersections of the unstable (magenta) and stable (blue) manifold returns of the L_1 and L_2 Lyapunov orbits, respectively, are indicative of a heteroclinic connection between the two orbits. The Poincaré section in Figure 9(b) highlights several such intersections and, as an illustrative example, the intersection highlighted in Figure 9(c) is selected. The full 6-dimensional state is then propagated forwards and backwards in time, resulting in a natural, maneuver-free transfer path that provides a direct connection between the L_1 and L_2 Lyapunov orbits. The transfer appears in Fig-

ure 10(a), where the magenta arc indicates departure from the L_1 Lyapunov orbit, which then flows into the blue arc, i.e., the stable manifold trajectory approaching the L_2 Lyapunov orbit.

A heteroclinic chain is then also constructed by linking the L_1-DPO heteroclinic connection with the DPO-L_2 Lyapunov heteroclinic connection. Thus, intersections of the unstable (magenta) and stable (teal) manifold returns of the L_1 Lyapunov orbit and the DPO, respectively, are sought. Similarly, the intersections of the unstable (yellow) and stable (blue) returns of the DPO and the L_2 Lyapunov orbit, respectively, supply the second leg of the heteroclinic chain. By selecting returns for the L_1-DPO and DPO-L_2 legs that lie close to original L_1-L_2 heteroclinic connection, relationships between the invariant manifolds of the three orbits are revealed.[11] Thus, the intersections that are evident in the zoomed-in view in Figure 9(c) are selected here as well. The complete heteroclinic chain is illustrated in Figure 10(b), where the magenta and teal arcs represent the L_1-DPO heteroclinic connection, and the yellow and blue arcs represent the DPO-L_2 leg of the chain. The geometries in Figure 10(a) and Figure 10(b) are inherently the same, confirming the relationship between the invariant manifolds of the orbits at this energy level. A return trajectory going from the L_2 Lyapunov orbit to the L_1 Lyapunov is also possible by leveraging the unstable manifold of the L_2 Lyapunov and the stable manifold of the L_1 Lyapunov orbit, respectively. Additionally, combining the L_1-L_2 or the L_1-DPO-L_2 chains with the associated return sequence produces an L_1-L_2-L_1 or L_1-DPO-L_2-DPO-L_1 pathway that is an orbit by itself. Thus, orbits that pass back and forth between the near and far sides of the Moon are computed. By recognizing the inherent relationships between the known orbits in the CR3BP, new periodic orbits that combine the geometries of the underlying orbits and possess desirable geometries are yielded.

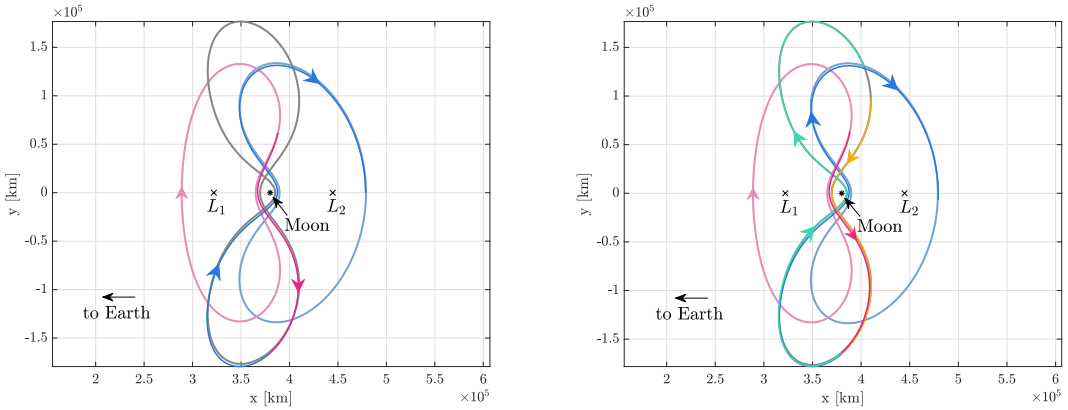

(a) L_1-L_2 Heteroclinic Connection

(b) L_1-DPO-L_2 Heteroclinic Chain

Figure 10. Heteroclinic connection and heteroclinic chain between the selected L_1 and L_2 Lyapunov orbits, $C = 2.97895$.

Similar cost-free links between the L_1 and L_2 Lyapunov orbits also exist at higher values of Jacobi constant, under the condition that the DPOs at that energy level are unstable. Consider the characteristics of the L_1 and L_2 Lyapunov orbits and the DPO in Table 2, all at the Jacobi constant value of $C = 3.11295$. Note that the stability indices associated with the Lyapunov orbits increased significantly, while the DPO is considerably less unstable in this case. This behavior is consistent with the evolution of the stability indices illustrated in Figure 3(a). Despite the relative reduction in the stability index, the stable and unstable manifolds of the DPO do exist at this energy level and are leveraged to construct the two legs of the L_1-L_2 heteroclinic chain. A heteroclinic

connection between the L_1-L_2 orbits appears in Figure 11(b), where the magenta arc lies on the unstable manifold of the L_1 Lyapunov orbit and, thus, asymptotically departs the orbit, and the blue arc lies on the stable manifold of the L_2 Lyapunov orbit and approaches the orbit when propagated forwards in time. Similarly, intersections of the unstable manifold (magenta) and stable manifold (teal) of the L_1 Lyapunov orbit and the DPO, respectively, yield an L_1-DPO heteroclinic connection; the unstable manifold (yellow) and stable manifold (blue) of the DPO and the L_2 Lyapunov intersect at a DPO-L_2 heteroclinic connection. Combining the two, an L_1-DPO-L_2 heteroclinic chain is produced and is represented in Figure 11(c). As is evident from Figure 11, adopting two different approaches (L_1-L_2 and L_1-DPO-L_2) yields similar transfer geometries. In this case as well, a return transfer geometry exists that departs the L_2 orbit and arrives at the L_1 Lyapunov orbit. Thus, the relationship between the invariant manifolds of the three orbits is maintained at this energy level as well.

Table 2. Characteristics of the selected orbits at $C = 3.11295$.

Orbit	Period (days)	Stability Index	Cone Angle (°)
L_1 Lyapunov	13.22	641.762	9.28
L_2 Lyapunov	15.37	408.083	7.41
DPO	12.80	74.704	8.304

Transfers between L_2 Lyapunov and 2:1 Retrograde Resonant Orbits

The Lyapunov orbits are local in the vicinity of the Moon; the 2:1 resonant orbit in Figure 7 is much larger and links the vicinity of the Moon with GEO. Access from the lunar far side into the 2:1 resonance is then facilitated through L_2 Lyapunov orbits. Since these L_2 orbits are also planar, transfer arcs that lie in the Earth-Moon plane are sought. As previously mentioned, the Jacobi constant range for the 2:1 retrograde resonant orbit family is significantly low compared to other periodic orbits in the Earth-Moon system and, thus, natural cost-free transfers into these orbits do not exist. However, the methodologies introduced in the construction of the heteroclinic chains are extended to provide access to the resonant orbits for reasonable costs and times of flight. Based on the selection of the departure orbit from within the L_2 Lyapunov family, two possible transfer options are introduced: i) transfers incorporating L_2 Lyapunov and DPO manifold arcs, and ii) transfers incorporating DPOs as transfer arcs.

As the difference in the magnitude of the Jacobi constant values for the departure and arrival orbits increases, the theoretical minimum ΔV required to transfer between them increases as well.[19] Thus, for the same arrival orbit, departures from lower amplitude (higher Jacobi constant) L_2 Lyapunov orbits are expected to require larger maneuver costs. For the first example, consider departure from an L_2 Lyapunov orbit at the Jacobi constant value of $C = 2.97895$, possessing a cone angle of approximately $\beta = 16.57°$. At this energy level, the L_2 Lyapunov orbit is unstable in a linear sense and, thus, possesses stable and unstable manifolds that arrive at and depart from the orbit asymptotically. From the family of 2:1 retrograde resonances, the arrival orbit is selected such that it is tangent to the altitude of a GEO as it approaches the Earth in a retrograde direction, at $C = 0.8964$. The two orbits are illustrated together in Figure 12(a) as seen in the Earth-Moon rotating frame.

The relationship between the invariant manifolds of the libration point orbits and the DPOs that became apparent due to the existence of heteroclinic chains is leveraged here to construct transfer

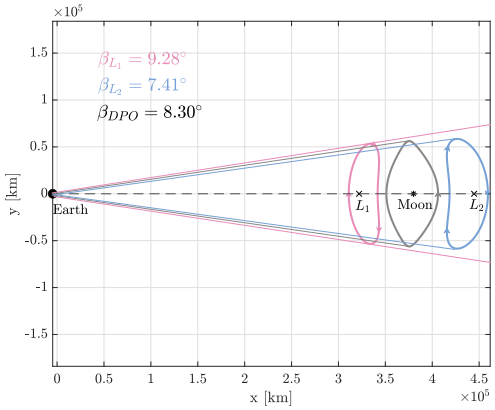

(a) Selected Orbits and Cone Angles

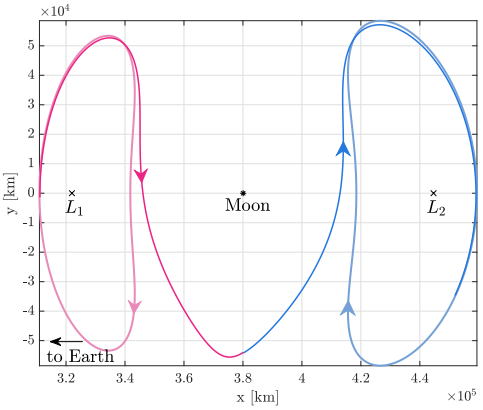

(b) L_1-L_2 Heteroclinic Connection

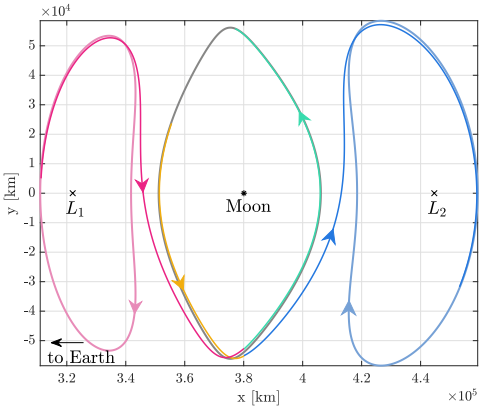

(c) L_1-DPO-L_2 Heteroclinic Chain

Figure 11. Heteroclinic connection and heteroclinic chain between the selected L_1 and L_2 Lyapunov orbits, $C = 3.11295$.

arcs that connect the L_2 Lyapunov orbit with the 2:1 resonant orbit. Thus, also appearing in Figure 12(a) is a DPO computed at the same Jacobi constant value as the L_2 Lyapunov orbit, passing approximately $5,200\ km$ from the center of the Moon. The cone angle associated with the DPO is approximately $24.66°$. Contrary to the construction of the first heteroclinic chains, in this case, trajectories that lie on the *unstable* manifold of the L_2 Lyapunov orbit and on the *stable* manifold of the DPO are computed. Following that, a hyperplane is defined as $\Sigma : x = 1 - \mu$, again corresponding to the location of the Moon in the Earth-Moon rotating frame. The intersections of the trajectories with this hyperplane are recorded and are illustrated in Figure 12(b). The returns of the unstable manifold of the L_2 Lyapunov orbit appear in magenta, and the returns of the stable manifold of the DPO appear in teal. In this case as well, the intersections of the magenta and teal points represent heteroclinic connections between the L_2 Lyapunov orbit and the DPO. Picking one such intersection and propagating it forwards and backwards in time, a natural, cost-free transfer between the departure L_2 Lyapunov orbit and the DPO is produced. For the final leg of the transfer, to link with the arrival 2:1 resonant orbit, it is noted that this particular DPO is tangent to the 2:1 resonance on the near side of the Moon. Thus, a tangential ΔV is applied at the point of tangency to complete transfer from the DPO to the 2:1 resonant orbit. Of course, the maneuver simply bridges

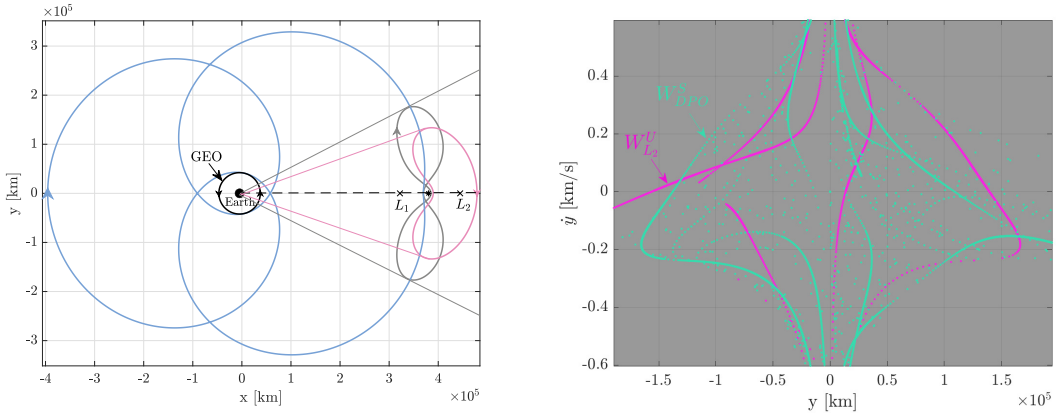

(a) Selected Orbits (b) Poincaré Section

Figure 12. Selected orbits and Poincaré section with returns of trajectories moving along invariant manifolds of the orbits.

the energy gap between the two orbits and reflects the lowest possible cost.

A multiple shooting scheme is employed to ensure continuity in position and velocity along the transfer arcs identified from the Poincaré map. The complete transfer trajectory is illustrated in Figure 13(a). Departure from the L_2 Lyapunov orbit is represented via the magenta arc, which eventually intersects with the trajectory on the stable manifold of the DPO, as represented in teal. A ΔV equal to $801.05\ m/s$ is applied at the tangential intersection of the teal arc with the 2:1 resonant orbit, completing the transfer trajectory. A zoomed-in view of the transfer trajectory near the Moon is plotted in Figure 13(b). The time of flight along the transfer path is approximately $25.92\ days$. This transfer reflects pathways connecting the lunar far side to the near-Earth realm, approaching a GEO in the retrograde direction.

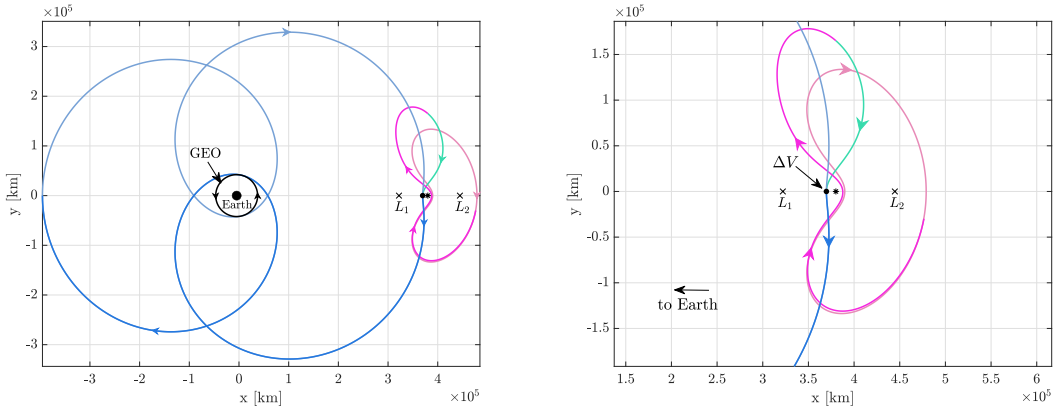

(a) Overview of the Transfer (b) Zoomed-in View

Figure 13. Transfer from an L_2 Lyapunov orbit to 2:1 retrograde resonant orbit.

The second possible strategy for a transfer into the 2:1 resonances from the lunar back side arises when departures from low-amplitude (relative to the Moon) L_2 Lyapunov orbits are considered,

which possess higher values of Jacobi constant. Additionally, at the higher Jacobi constant level, the DPOs tend to be stable or nearly stable in a linear sense and, thus, lack useful manifold structures. As a result, transfers incorporating L_2 Lyapunov and DPO manifold arcs are not available. In such cases, an option for feasible transfers simply involves leveraging DPOs as intermediate transfer arcs. Consider, then, departure from an L_2 Lyapunov orbit with $C = 3.1490$ that passes $49,800\ km$ from the Moon. As a comparison, the arrival orbit is selected as the same 2:1 retrograde resonance as the previous example, i.e., the resonant orbit with $C = 0.8964$. As noted previously, for the same arrival orbit, the higher Jacobi constant value for the departure orbit predicts higher transfer costs as well. To link the two orbits, a DPO is computed such that it tangentially intersects both the departure L_2 Lyapunov orbit and the 2:1 resonant orbit. The resulting DPO possesses a Jacobi constant value of $C = 3.1718$. A tangential maneuver at the intersection of the L_2 Lyapunov and the DPO, denoted ΔV_D, is applied to depart the orbit and is approximately equal to $75.91\ m/s$. An arrival maneuver, ΔV_A, is applied at the intersection of the DPO with the 2:1 resonant orbit, equal to $915.54\ m/s$. Thus, the total ΔV required for the transfer is $991.45\ m/s$, with a time of flight equal to half the period of the intermediate DPO, about $4.54\ days$. Predictably, the larger energy differences in this case necessitates a higher cost of transfer. However, leveraging a DPO as an intermediate transfer arc significantly reduced the time of flight of the transfer. In this example as well, the maneuvers are tangential and bridge the energy gaps between the orbits. Because of the choice of the DPO, the departure maneuver, ΔV_D, *increases* the Jacobi constant value from 3.1490 to 3.1718. The arrival maneuver, ΔV_A, that links the DPO with the 2:1 resonant orbit *decreases* the Jacobi constant, going from 3.1718 to 0.8964. Thus, for this set of orbits, the transfer costs is as low as possible, but utilizing other intermediate orbits besides the DPO might result in lower ΔVs.

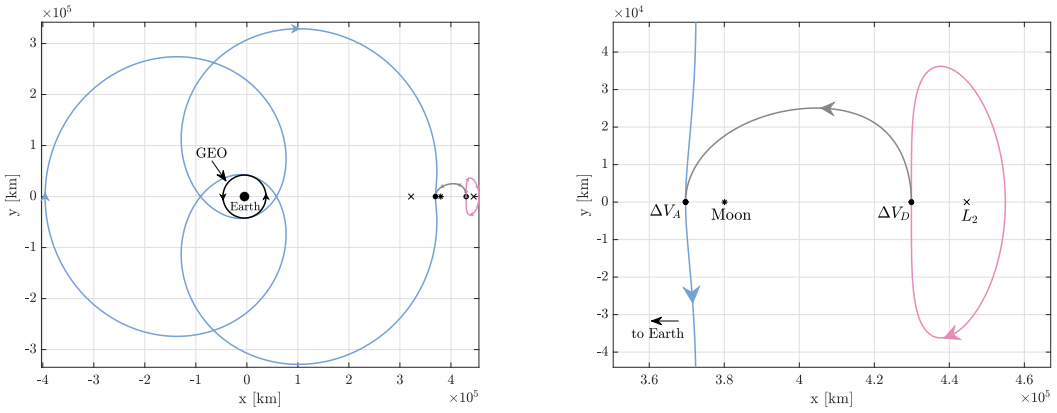

(a) Overview of the Transfer

(b) Zoomed-in View

Figure 14. Transfer from an L_2 Lyapunov orbit to 2:1 retrograde resonant orbit.

CONCLUDING REMARKS

Resonant orbits offer options for cislunar surveillance. In particular, the naturally precessing geometries of the 2:1 resonant orbits are potentially useful for the long-term monitoring of cislunar space. Libration point orbits and the Moon-centered distant prograde orbits (DPOs) offer possible local coverage in the lunar vicinity. These are incorporated in the design of maneuver-free heteroclinic connections between the L_1 and L_2 Lyapunov orbit families. Poincaré mapping reveals relationships between the invariant manifolds of these Lyapunov orbits and the DPOs at certain energy

levels. Additionally, heteroclinic chains that exhibit the geometries of all the underlying unstable periodic orbits are constructed. The heteroclinic chains yield repeating orbits in their own right that flow between the far and near sides of the Moon. The techniques presented here for the computation of planar heteroclinic chains are extendable to the computation of their three-dimensional counterparts. In addition to providing lunar coverage, spatial orbits possessing similar geometries would permit direct communication with the Earth and provide access to the near-Earth realm.

The low values of Jacobi constant in the 2:1 resonant orbit family reflect the high energy of such orbits to pass through much of cislunar space. The expected lack of natural dynamical structures in the Earth-Moon system at these low Jacobi constant levels presents challenges associated with accessing the orbits from the lunar vicinity. However, the relationship between the invariant manifolds of the libration point orbits and the DPOs introduces transfer options that connect the lunar far side with the resonant orbits. For low-Jacobi constant departures from the far side of the Moon, invariant manifolds associated with the L_2 Lyapunov orbits and the DPOs are incorporated to gain access to the 2:1 resonant orbits. For high-Jacobi constant departures, the lack of useful invariant manifolds is addressed by incorporating distant prograde orbits as intermediate transfer arcs. The proposed transfer options link the lunar vicinity to the geostationary region, thereby aiding active surveillance of cislunar space.

ACKNOWLEDGEMENTS

The authors would like to thank the Purdue University School of Aeronautics and Astronautics for supporting this work. The authors appreciate access to the computational facilities at the Barbara and Rune Eliasen Visualization Laboratory. Meaningful discussions with the members of the Multi-Body Dynamics Research Group at Purdue University are also highly appreciated.

REFERENCES

[1] C. Trentlage and E. Stoll, "A Biomimetic Docking Mechanism for Controlling Uncooperative Satellites on the ELISSA Free-Floating Laboratory," *2018 3rd International Conference on Advanced Robotics and Mechatronics (ICARM)*, 07 2018, pp. 77–82.

[2] C. Frueh, K. Howell, K. DeMars, and S. Bhadauria, "Cislunar Space Situational Awareness," *31st AIAA/AAS Space Flight Mechanics Meeting*, 2021.

[3] J. Ruhe, "SDA's Kennedy: Cislunar Space The Next Military Frontier," April, 2019. https://breakingdefense.com/2019/04/sdas-kennedy-cislunar-space-the-next-military-frontier/, last accessed at 2021-04-20.

[4] C. Frueh, K. Howell, K. DeMars, S. Bhadauria, and M. Gupta, "Cislunar Space Traffic Management: Surveillance through Earth-Moon Resonance Orbits," *8th European Conference on Space Debris*, 2021.

[5] D. Craig Davis and K. C. Howell, "Trajectory Evolution in the Multi-Body Problem with Applications in the Saturnian System," *Acta Astronautica*, 2011, 10.1016/j.actaastro.2011.07.007.

[6] B. P. McCarthy and K. C. Howell, "Leveraging Quasi-Periodic Orbits for Trajectory Design in Cislunar Space," *Astrodynamics*, 2021, 10.1007/s42064-020-0094-5.

[7] M. W. Lo, B. G. Williams, W. E. Bollman, D. Han, Y. Hahn, J. L. Bell, E. A. Hirst, R. A. Corwin, P. E. Hong, K. C. Howell, B. Barden, and R. Wilson, "Genesis Mission Design," *AIAA/AAS Astrodynamics Specialist Conference and Exhibit*, 1998, 10.1007/bf03546342.

[8] A. F. Haapala, M. Vaquero, T. A. Pavlak, K. C. Howell, and D. C. Folta, "Trajectory Selection Strategy for Tours in the Earth-Moon System," *Advances in the Astronautical Sciences*, 2014.

[9] D. C. Folta, T. A. Pavlak, A. F. Haapala, K. C. Howell, and M. A. Woodard, "Earth-Moon Libration Point Orbit Stationkeeping: Theory, Modeling, and Operations," *Acta Astronautica*, 2014, 10.1016/j.actaastro.2013.01.022.

[10] E. Zimovan, "Characteristics and Design Strategies for Near Rectilinear Halo Orbits within the Earth-Moon System," M.S. Thesis, Purdue University, West Lafayette, Indiana, 2017.

[11] M. Vaquero, *Spacecraft Transfer Trajectory Design Exploiting Resonant Orbits in Multi-Body Environments*. PhD thesis, Purdue University, West Lafayette, Indiana, 2010.

[12] C. Murray and S. Dermott, *Solar System Dynamics*. Two Volumes, Cambridge University Press, Cambridge, United Kingdom, 1999.

[13] J. G. Peterson, J. P. Carrico, R. DeMajistre, N. Schwadron, K. Fairchild, C. Reno, and R. Vanderspek, "Science Operations Support for the Orbit Change on the Interstellar Boundary Explorer (IBEX) Mission," *IEEE Aerospace Conference Proceedings*, 2012.

[14] M. Vaquero, "Poincaré Sections and Resonant Orbits in the Restricted Three-Body Problem," M.S. Thesis, Purdue University, West Lafayette, Indiana, 2010.

[15] M. Holtzinger, C. Chow, and P. Garretson, "A Primer on Cislunar Space," AFRL Space Vehicles Directorate, AFRL 2021-1271. June, 2021.

[16] R. W. Farquhar, "The Utilization of Halo Orbits in Advanced Lunar Operations," *NASA X-551-70-449, GSFC, Greenbelt*, 1971.

[17] W. Schlei, *Interactive Spacecraft Trajectory Design Strategies Featuring Poincaré Map Topology*. PhD thesis, Purdue University, West Lafayette, Indiana, 2017.

[18] T. Hitchens, "AFRL Satellite To Track Up To The Moon; Space Force-NASA Tout Cooperation," September, 2020. https://breakingdefense.com/2020/09/afrl-satellite-to-track-up-to-the-moon-space-force-nasa-tout-cooperation/, last accessed at 2021-07-27.

[19] M. Gupta, "Finding Order in Chaos: Resonant Orbits and Poincaré Sections," M.S. Thesis, Purdue University, West Lafayette, Indiana, 2020.